Dynamic Microwave Imaging of the Cardiovascular System Using Ultra-Wideband Radar-on-Chip Devices

Timo Lauteslager, Mathias Tømmer, *Student Member, IEEE*, Tor S. Lande, *Fellow, IEEE*, and Timothy G. Constandinou, *Senior Member, IEEE*

Abstract*—*Objective: **Microwave imaging has been investigated for medical applications such as stroke and breast imaging. Current systems typically rely on bench-top equipment to scan at a variety of antenna positions. For dynamic imaging of moving structures, such as the cardiovascular system, much higher imaging speeds are required than what has thus far been reported. Recent innovations in radar-on-chip technology allow for simultaneous high speed data collection at multiple antenna positions at a fraction of the cost of conventional microwave equipment, in a small and potentially portable system. The objective of the current work is to provide proof of concept of dynamic microwave imaging in the body, using radar-on-chip technology. *Methods:* Arrays of body-coupled antennas were used with nine simultaneously operated coherent ultra-wideband radar chips. Data were collected from the chest and thigh of a volunteer, with the objective of imaging the femoral artery and beating heart. In addition, data were collected from a phantom to validate system performance. Video data were constructed using beamforming. *Results:* The location of the femoral artery could successfully be resolved, and a distinct arterial pulse wave was discernable. Cardiac activity was imaged at locations corresponding to the heart, but image quality was insufficient to identify individual anatomical structures. Static and differential imaging of the femur bone proved unsuccessful. *Conclusion:* Using radar chip technology and an imaging approach, cardiovascular activity was detected in the body, demonstrating first steps towards biomedical dynamic microwave imaging. The current portable and modular system design was found unsuitable for static in-body imaging. *Significance:* This first proof of concept demonstrates that radar-on-chip could enable cardiovascular imaging in a low-cost, small and portable system. Such a system could make medical imaging more accessible, particularly in ambulatory or long-term monitoring settings.**

***Index Terms*—Biomedical imaging, cardiovascular, microwave imaging, radar-on-chip, ultra-wideband radar.**

I. Introduction

MICROWAVE imaging (MWI) microwave imaging (MWI) is increasingly being investigated for use in medicine: Multiple imaging systems have undergone clinical trials for breast imaging [1] and commercial efforts are under way to test microwave stroke imaging [2]. The use of microwave technology is of interest because of its non-ionizing properties, meaning that it can safely be used for sensing and imaging in the body. Microwave radiation penetrates biological tissue reasonably well, and contrasts exist between various tissues. In addition, MWI systems typically rely on relatively low-cost equipment. MWI in the body is enabled by the contrast in intrinsic impedance between biological tissues: As electromagnetic (EM) waves at microwave frequencies impinge on boundaries between tissues, scattering, reflection and transmission of EM energy will occur. The rate of reflection and transmission depends on the difference between each tissue's impedance, which in turn is determined by their dielectric properties. Dielectric properties of tissues are, amongst other factors, greatly affected by water content [3], which enables for example detection of tumour tissue in adipose breast tissue [1]. two-dimensional (2D) or three-dimensional (3D) imaging of a body's composition relies on the radiation of microwaves into the body using a transmitter (Tx) antenna, and capturing scattered energy at various receiver (Rx) antenna locations. Often, one or two antennas may be used to scan through a variety of physical locations to acquire a spatially diverse dataset (typically referred to as synthetic aperture, as shown in [4], [5]). Alternatively, a static array of antennas is used (real aperture, as demonstrated in [6], [7]). As data acquisition is limited by the number of ports available on a vector network analyser (VNA), scanning of a static array may be done by electronic switching between antenna channels. For image formation, two alternative approaches are used: Microwave tomography and ultra-wideband (UWB) radar imaging. Microwave tomography (as employed by [8] and [9] for breast imaging and brain imaging, respectively) is a quantitative approach, and attempts to reconstruct the dielectric

Manuscript received 8 August 2021; revised 22 January 2022 and 3 March 2022; accepted 6 March 2022. Date of publication 10 March 2022; date of current version 22 August 2022. This work was supported in part by an EPSRC DTA scholarship. *(Corresponding author: Timo Lauteslager.)*

Timo Lauteslager is with the Centre for Bio-Inspired Technology, Department of Electrical and Electronic Engineering, Imperial College London, SW7 2AZ London, U.K. (e-mail: timolauteslager@gmail.com).

Mathias Tømmer and Tor S. Lande are with the Department of Informatics, University of Oslo, Norway.

Timothy G. Constandinou is with the Centre for Bio-Inspired Technology, Department of Electrical and Electronic Engineering, Imperial College London, U.K. and also with the Care Research and Technology Centre (Dementia Research Institute), Imperial College London, U.K.

Digital Object Identifier 10.1109/TBME.2022.3158251

profile of the anatomy by solving the ill-posed inverse scattering problem. UWB radar imaging on the other hand, is a qualitative method. It utilizes wideband EM pulses to detect and determine the range of significant scatterers located in the anatomy. By combining spatially diverse UWB radar data, the location of a scatterer can be determined in 2D or 3D space (as demonstrated in [4], [6], [7], [10]–[12] for breast imaging, or in [5] for head imaging). Compared to microwave tomography, radar imaging algorithms are considered simple and robust. In addition, through time-gating, the use of a wide frequency band provides better resistance against multipath propagation interference than the often used narrowband signals in the case of microwave tomography.

Thus far, the medical application of MWI has been limited, with the majority of research focusing on either breast cancer imaging [4], [6], [7], [10]–[12] or stroke imaging [5], [9]. With cardiovascular disease being the leading cause of death globally, MWI could prove to be a valuable tool for monitoring the mechanics of the heart and the vascular system. Previously, one-dimensional (1D) sensing using UWB radar has been demonstrated for measuring arterial dynamics [13], for heart wall velocity [14], and for heart rate [15]. Potential applications of clinical relevance are blood pressure estimation from the arterial pulse wave (as shown in [16]), or for assessing the mechanical functioning of both the heart and arteries, where MWI could act a complementary method or alternative to ultrasound. MWI of the cardiovascular system poses a problem however: High scanning speeds are required to sample the cardiac dynamics at a sufficient frame rate, but Tx-Rx antenna pairs are typically scanned sequentially. This time-consuming process limits an imaging system's frame rate, and reduces temporal accuracy of the dynamic signal. Full-image scanning times of existing systems range from 5 seconds (using a very small 6-element antenna array [17]) to 30 minutes (for 200 scanning positions [4]). Only one attempt has been made at cardiac imaging using radar: A 2D time lapse movie of heart motion has been composed from successive radar images synchronized with electrocardiography (ECG) data [18], verifying that heart motion does modulate radar signals. A high cost VNA was used in combination with a switch matrix, but the constraint of short scanning times reduced both the VNA sensitivity and the radar down range resolution, and true dynamic imaging has not been demonstrated.

Recent innovations in integrated circuit radar sensors may unlock high-speed dynamic MWI, without sacrificing sensitivity and resolution. A complete UWB radar transceiver system may fit on a chip the size of a fingernail. Importantly, several such radar-on-chip (RoC) systems can be used simultaneously to capture data at multiple antennas. This avoids the need for switching arrays, and speeds up data acquisition by a factor that equals the number of RoC systems. Thus dynamic imaging of moving structures in the body becomes a possibility.

The current work describes the first demonstration of dynamic MWI of the cardiovascular system, using a system of synchronized, coherent RoC devices. Imaging is performed both on the heart and on the femoral artery of a single human volunteer, as well as on a phantom object.

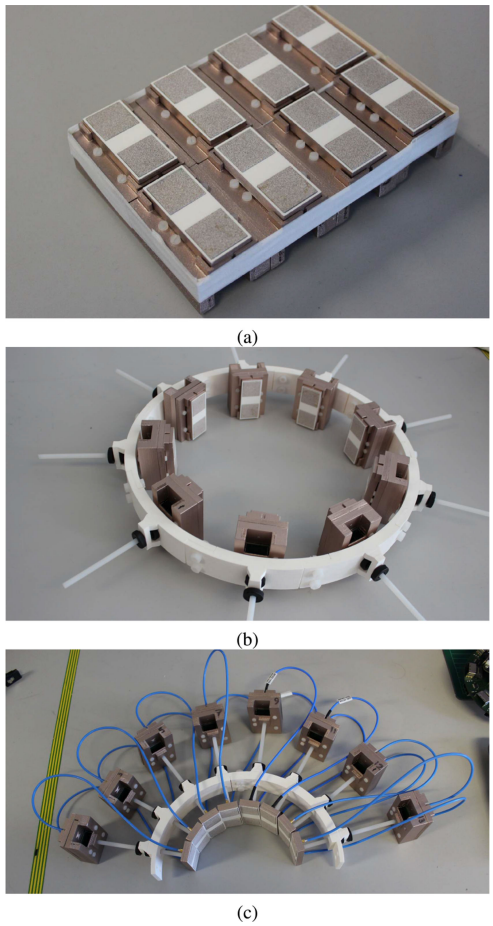

(a) (b) (c)

Fig. 1. Arrays of up to nine radar-on-chip modules and sets of body-coupled antennas, in three different configurations: Rectangular array (a), circular array (b), and semicircular array (c).

II. Methods

Imaging was performed using a portable system of synchronized coherent UWB RoC modules and body-coupled antennas in three array configurations, both on the human body and on a tissue-mimicking phantom. For human recordings, ECG data were recorded simultaneously. Recordings were made on the chest and the left thigh of a single participant, with the purpose of performing dynamic imaging of the heart and femoral artery. Static imaging was performed on data collected at the thigh, with the aim of imaging the femur bone. The objective of the phantom recording was to test static imaging in a controlled environment. For this purpose, a homogeneous, semi-solid phantom was constructed to mimic the dispersive dielectric properties of biological tissue. An oil-in-gelatin dispersion was created [19], [20] to resemble high water-content tissue. Steel rods were used as high-contrast imaging targets. Three arrays of RoC modules and body-coupled antennas were constructed (pictured in Fig. 1): Circular, semicircular, and rectangular. The three measurement scenarios (thigh, chest, and phantom), as well as array placements relative to the imaging object and the different recording conditions are illustrated in Fig. 2.

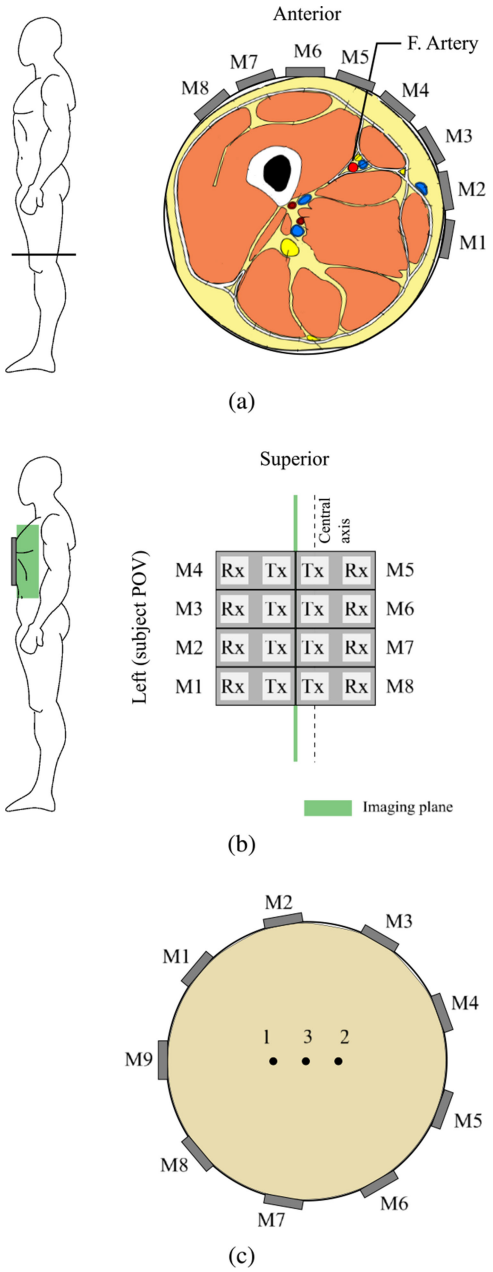

Fig. 2. Schematic illustration of the three experimental conditions: Imaging of the femoral artery on the left lower thigh of a volunteer (a); imaging of the heart using a rectangular array pressed on the chest (c); and imaging of up to three targets (steel rods with 5 mm diameter) in a cylindrical tissue-mimicking phantom (c). For thigh and phantom imaging, both the circular array and semicircular array were used.

A. Radar-on-Chip Imaging System

1) Radar Modules: Up to nine RoC modules were operated simultaneously. Each module consisted of the XeThru X2 single-chip UWB radar transceiver (Novelda AS, Kviteseid, Norway), with additional amplifiers in the transmit and receive signal paths to improve sensitivity, as well as a 2.5 GHz highpass filter to reduce out-of-band interference. The transmitted waveform is a fully coherent, approximated Gaussian modulated sinusoid with adjustable center frequency. In this work, the lowest possible center frequency of 3.45 GHz was selected (to reduce signal absorption at the cost of cross-range resolution), with –10 dB bandwidth of 2.5 GHz, and pulse width (–3 dB) of 1 ns. The X2 achieves an effective sample rate of approximately 40 GHz using swept threshold single bit quantization. A 13 b digital-to-analog converter is used to set the threshold, and the single bit quantization result is distributed to 256 counters. A tapped delay line is used to trigger the counters sequentially, with a timing difference of approximately 25 ps, resulting in an equivalent sampling rate of 40 GHz and a sampling window of approximately 6.4 ns. The threshold is swept over the range of the input signal. The threshold sweep is repeated to improve signal-to-noise ratio (SNR) through averaging [21]. Each radar module was enclosed in a 3D printed box, constructed from conductive graphene filament and spray-painted in conductive paint to improve shielding. Each module is connected to a motherboard which distributes power, data buses and a high quality trigger signal to synchronize the radar modules, enabling coherent operation. A single board computer is used for radar communication, control and data aggregation.

2) Body-Coupled Antennas: Each radar module connected to one Tx and one Rx antenna. Body-coupled wideband monopole antennas of 2 by 2 cm were constructed, with measured –10 dB reflection bandwidth of 2.5–7.0 GHz on various body parts. Low-loss dielectric spacers (Eccostock HIK500F) of 2.5 mm thickness and permittivity roughly matching the skin ($\varepsilon_r \approx 30$) were placed over the antenna surface to reduce losses in the near field, and improve radiation into tissue: A 6 dB performance improvement was found on in-vivo transmissive measurements. Further details on body-coupled antenna design and performance are published in [22]. Pairs of antennas were held in place using 3D printed fixtures, with a Tx-to-Rx distance (center to center) of 3.0 cm. Antenna fixtures were spray-painted using silver-coated copper conductive paint to improve shielding. Antenna fixtures could be fitted into the radar module boxes, with antennas directly connecting to the radar modules via SMP snap connectors. Because of the physical dimensions of the radar module box (4.0 by 5.7 cm), a dense array could not be created with the module box directly adjacent to the antenna fixture. To achieve higher antenna density, antenna connectors were extended using SMP cables in case of the semicircular array [see Fig. 1(c)].

3) Radar Module Arrays: Radar modules boxes and antenna fixtures were fixed in 3D printed arrays. The circular array consisted of a ring with nine adjustable radar module attachment points, providing a 360° coverage around circular imaging geometries. The array provided an adjustable inner antenna array diameter ranging from 11.0 to 16.0 cm. The lowest possible inter-antenna distance was 3.8 cm. The semicircular array used a similar bolt positioning system, with only the antenna fixtures attached, so that an inter-antenna spacing of 2.0 cm could be achieved at an array diameter of 11.0 cm. Eight sets of antennas and radar modules were mounted into the rig, spanning an angular coverage of 144°. The rectangular array consisted of eight module boxes with antenna fixtures, attached in a four-by-two grid. Array density was limited by module box dimensions, providing an inter-module distance of 4.0 cm and 5.7 cm. Total array aperture (measured at centers of outermost antennas) was 8.7 by 12.0 cm.

4) Imaging Mode: All radar modules received simultaneously, with a single module acting as transmitter. The Tx module could be held constant to collect single-input and

multiple-output (SIMO) data, or the Tx function could be rotated between all modules to synthetically construct a multiple-input and multiple-output (MIMO) dataset.

5) Electrocardiography: To provide a reference for heart cycle timing, ECG data were recorded at a sample rate of 250 Hz, using an Arduino and Olimex ECG shield. ECG data were recorded between two electrodes on the chest, just inferior to the left and right clavicle, using a left lower rib cage electrode as reference.

B. Measurement Procedures

All in-human recordings were performed on a single volunteer. The male participant was 29 years of age, had a body mass index (BMI) of 20.5, and reported no cardiovascular disease. Approval for the study was obtained from the Imperial College London institutional ethics committee (SETREC approval ref: 19IC5232).

1) Thigh Imaging: The circular and semicircular arrays were used for thigh measurements, both at the lower left thigh. Antennas were tightly pressed against the skin. For the semicircular array, an elastic band was used to ensure that the array was pressed tightly onto the skin. Array orientation relative to anatomy is illustrated in Fig. 2(a). For each condition, 60 s of data were recorded. During recordings, the participant was comfortably seated and asked to minimize movement. Apart from MIMO data, SIMO data were also recorded with the module which was hypothesized to be nearest to the femoral artery acting as transmitter.

2) Heart Imaging:: The rectangular array was used for chest measurements. Array positioning is specified in Fig. 2(b). The antenna array was placed on a flat surface, antennas facing upwards, with the participant lying on the array in prone position. This ensured a static array position during the recording as well as good antenna-skin contact. For each recording, 60 s of data were collected both while the participant was breathing and while holding breath. During recordings, the participant was asked to minimize movement.

3) Phantom Imaging: Circular and semicircular arrays were used for phantom measurements. Antennas were tightly pressed against the cylindrical phantom. In the case of the semicircular array, an elastic band was used to ensure that the array was pressed on the phantom surface. Throughout experiments, a single phantom was used, with and without targets. First, an 'empty' recording was performed without targets inserted. Then, up to three metal rods (5 mm diameter) acted as targets and were inserted in the phantom (circular array) or extracted from the phantom (semicircular array) between recordings, as shown in Fig. 2(c).

C. Medium Properties

To ensure coherent summation, delay of received signals need to be modelled according to propagation path length and medium properties. Signal attenuation and propagation velocity is estimated from a medium's dielectric properties: relative permittivity ε_r and conductivity σ. Dielectric properties of the different media were measured (in case of the phantom), or taken from literature [23], assuming a center frequency of 3.45 GHz.

Fig. 3. Transverse cross section of human torso, illustrating the size and location of the heart [25].

TABLE I
ESTIMATED TISSUE FRACTIONS FOR THE CHEST AND THIGH

Tissue	Chest		Thigh
	Thickness [mm]	Fraction [%]	Cross-sectional area fraction [%]
Skin	2	5	5
Fat	5	12	15
Muscle	10	24	75
Bone	15	36	5
Lung	10	24	-

1) Chest Properties: Fig. 3 shows an example of a human torso cross section. The heart lies directly against the rib cage and is laterally surrounded by lung tissue. The propagation path of peripheral imaging channel paths include lung tissue, whereas central channel paths will contain more bone tissue. For the current work, a 1D homogeneous model of the path up until the heart wall is considered. Tissue layer thickness assumptions (based on [24], [25]) are given in Table I. A weighted average was used to estimate effective relative permittivity and conductivity at 25.1 and 1.33 S/m, respectively.

2) Thigh Properties: Thigh circumference was measured to be 40 cm. Thigh composition was estimated from [26], resulting in a thigh tissue cross-sectional fraction estimate as in Table I. A weighted average was used to estimate the effective relative permittivity and conductivity at 42.8 and 2.1 S/m, respectively.

3) Phantom Properties: The effective relative permittivity and conductivity of the constructed phantom were measured at 30.5 and 1.70 S/m, respectively, at 3.45 GHz. A two-pole Debye model was fitted to measured data, to allow modeling of frequency-dependent dielectric properties.

D. Imaging Algorithm

A schematic overview of the signal processing pipeline is given in Fig. 4, with data (D), processes (P) and outcomes (O) alphanumerically labelled and indicated using ellipses, rectangles and parallelograms, respectively.

1) Preprocessing:

a) Module Calibration Delay: A central trigger signal ensured coherent operation of all radar modules. System calibration was performed as follows: Module sampling delay offset (absolute delay within individual modules; D3 in Fig. 4) was calibrated to ensure a constant duration between pulse transmission and onset of sampling across modules, as verified using a Tx-to-Rx jumper cables. Module delay time calibration (delay

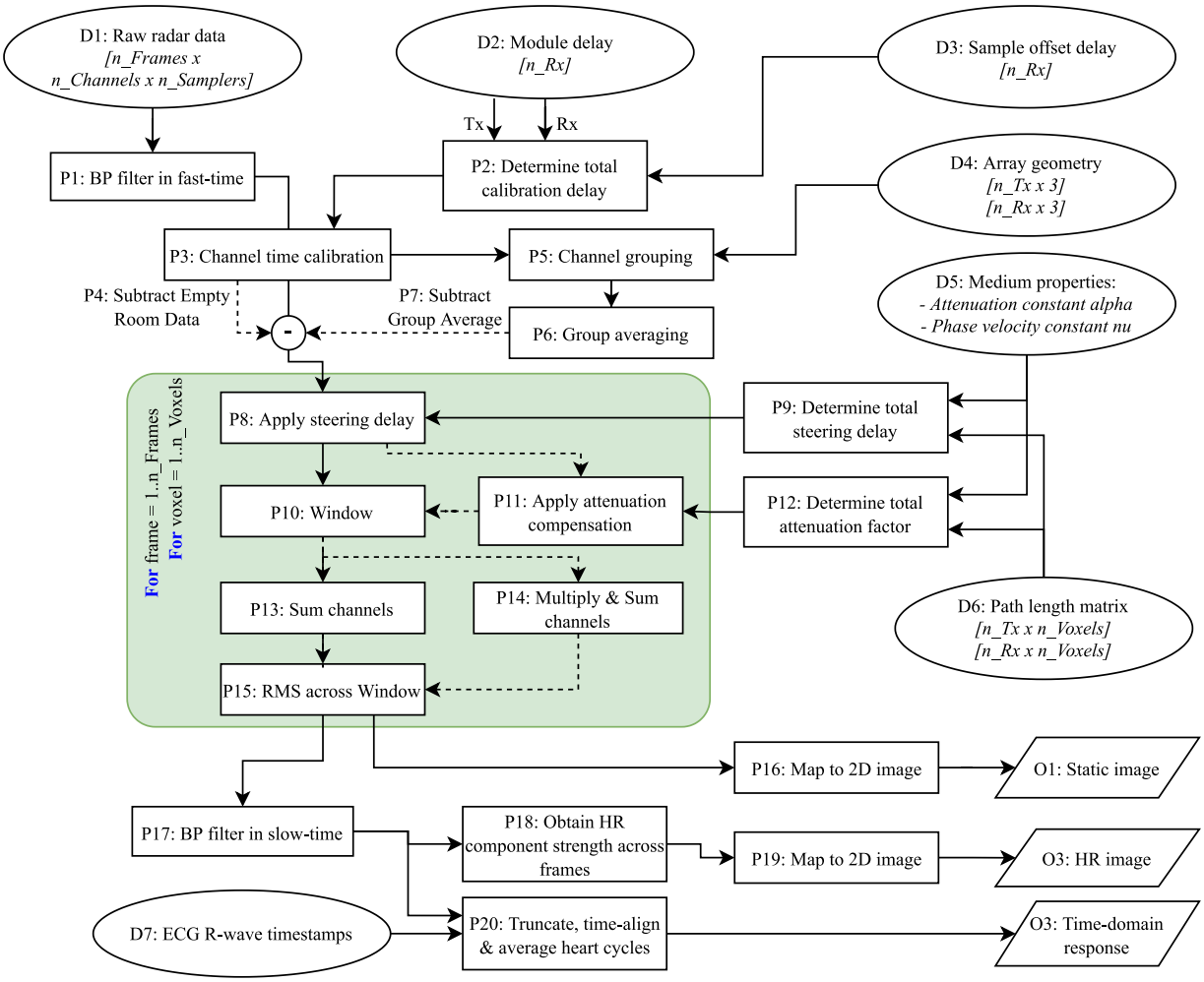

Fig. 4. Schematic pipeline of imaging algorithm. Ellipses, rectangles and parallelograms denote data (d), processes (p) and outcomes (o), respectively. Dashed lines denote an optional step.

between trigger signal and individual modules; D2) was performed to ensure synchronous operation between radar modules. A multistatic dataset in a circular antenna array was recorded, and any differences in pulse time-of-arrival between channels with identical path lengths were compensated for. Based on simulations of the effect of signal jitter on attenuation of summed coherent signals, an imprecision of up to 1 sampler was deemed acceptable in channel delay calibration (P3).

b) Filtering: Obtained radar frames (D1) were zero-phase bandpass filtered (P1) to eliminate DC offset and out-of-band noise. The continuous wavelet transform (analytical Morse wavelet) was chosen, as experimentation showed good resistance against high frequency signal smearing when applying path length attenuation compensation. The passband was determined by measuring the –30 dB bandwidth of the transmitted signal.

c) Clutter Removal: Suppression of strong clutter signals is key for successful image formation, as signal attenuation in tissue is high (∼7 dB/cm at a center frequency of 3.45 GHz) and clutter signals (skin boundary reflections, crosstalk) may be many times higher in amplitude. In this work, body-coupled antennas are used instead of the more common approach of a liquid coupling medium to reduce what is known as the 'skin artefact' [27], but static clutter arising from the skin boundary are not avoided altogether. Two separate approaches were taken to eliminate static clutter. In the presence of an 'empty room' dataset (phantom measurements), differential imaging was performed whereby the empty dataset was subtracted from the dataset with target (P4). When differential imaging was not possible (human body measurements), the skin artefact was estimated by averaging a group of channels with similar geometry. For this, the Euclidean distance between Tx and Rx element was determined for all channels, and channels were grouped according to distance (P5) and averaged (P6). Skin artefact removal was performed on each channel by subtracting the group average (P7). Because array imperfections could lead to minor signal phase shifts, the Woody average was applied: Cross-correlation between signals was optimized for, by iteratively changing a small delay applied to the input signals. The set of delays that resulted in the strongest cross-correlation was used to align and subtract the obtained clutter estimates.

2) Image Formation:

a) Beamforming: For near field imaging, beamformer delays are dependent on both direction of arrival (DOA) and target range. An imaging system must thus focus on individual

voxels in the target geometry. The simplest form of a delay-and-sum (DAS) beamformer can be written as [28]:

$$y(\mathbf{r}) = \left[\sum_{m=1}^{M} s_m(\tau_m(\mathbf{r}))\right]^2 \quad (1)$$

Where M represents the total number of Tx-Rx channels, and τ_m is the time delay for the path from Tx element position to focal point $\boldsymbol{r}$ back to Rx element position, for channel m (obtained in P9, from D5 and D6). Steering delays were applied in the time domain by truncation, with a precision of 1 sampler (P8). Instead of summing received signal s_m only at a single sampler corresponding to delay τ_m, a window around this sampler was chosen (P10), resulting in signal smoothing and increased imaging robustness. A window length of 5 samplers was used, which corresponds to 130 ps, or approximately $\frac{1}{2}\lambda$. This window length was found to be a good trade-off between SNR and robustness to error in the estimation of dielectric properties (as confirmed through simulations). An alternative to DAS, is the delay-multiply-and-sum (DMAS) algorithm. DMAS uses multiplication between channels to increase the number of signals before summation, thereby strongly reducing clutter, albeit it at a trade off of increased computation time [29]. In this work, DAS was used for beamforming on dynamic data (heart and artery imaging), implemented according to equation 1 (P13). For static imaging, consecutive frames could be averaged prior to beamforming, reducing the amount of data that required image formation processing. DMAS was therefore used for static image formation (P14). All 2D images were computed with 2 by 2 mm voxel size. Voxel intensity was determined as the root mean square (RMS) across the window length (P15).

b) Propagation Model: Successful image formation using DAS or DMAS relies heavily on the estimation of propagation velocity in the medium of interest. In addition, path length compensation may be performed to achieve unity gain for any voxel from any channel, and compensation of signal distortion may be required for coherent summation. The effect of dielectric dispersion at the considered bandwidth, propagation path lenghts, and media, was investigated through simulation and liquid phantom experiments (results not shown). Although a slight down-shift of pulse center frequency was observed, pulse distortion was found to be minimal, and dispersiveness could therefore be ignored. Thus, permittivity and conductivity were evaluated at the transmitted pulse center frequency (3.45 GHz), and steering delays could simply be applied in the time domain by truncation and concatenation of radar frames (P8). Compensation for signal attenuation was found to improve imaging performance for the rectangular array, but not in case of the circular array. Attenuation compensation (P11) was therefore applied to heart imaging data only.

c) Imaging Plane: The 2D rectangular array (used in heart imaging) allowed for visualisation of any plane a 3D space. Because of radar module size constraints, the planes along the array's x-axis (azimuth = 0°) and y-axis (azimuth = 90°) resulted in an undersampled array: Virtual element distance was around 2 cm, whereas the carrier wavelength in tissue is around 1.4 cm. It was found that a rotated imaging plane (adjusted azimuth) resulted in more desirable beamformer characteristics, with reduced spatial aliasing. It is also known that the human heart orientation is slightly slanted: The apex (most inferior part) of the heart is pointed towards the left downside. Two imaging planes were therefore chosen to align with the heart's long and short axis, at 23° and 113° counter-clockwise from the sagittal plane, respectively. Imaging plane rotation is illustrated in Fig. 5. Variations to imaging planes are accounted for in D4 and D6 in Fig. 4.

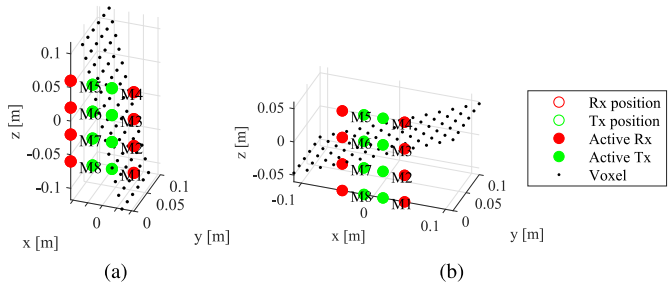

Fig. 5. Array and imaging plane geometry for the cardiac long axis plane (a); azimuth 113°) and short axis plane (b); azimuth 23°). A subset of voxels is shown to illustrate the imaging plane (at 2 cm spatial sampling).

d) Visualization: Static images (O1) were mapped to a 2D image (P16) and plotted as amplitude heatmaps on a logarithmic scale. In an analogy to ultrasound (US) imaging, 2D maps may be referred to as B-mode images. For dynamic imaging (O2), data were bandpass filtered in slow-time to remove low frequency drift and high frequency noise (P17). 2D visualization of obtained video data was done by generating heatmaps of signal amplitude at the heart rate (HR) frequency (obtained using the Fourier transform; P18), which was aimed to identify voxels with maximum cardiac activity. Besides the B-mode images, M-mode time-domain response plots (nomenclature from US imaging) were used to visualize time series of data at specific voxels (O3). To increase SNR, radar imaging frames and ECG data (D7) were aligned using fiducial ECG markers (R wave), and radar data over multiple heart cycles were averaged (P20).

e) Performance Evaluation: The following metrics were used to quantify performance:

1) The signal-to-clutter ratio (SCR) is defined as the logarithmic ratio of signal strength at a predefined voxel or set of voxels, to signal strength at all other voxels.
2) The location error is defined as the Euclidean distance between the heatmap maximum and true target location.

III. Results

A. Thigh Imaging

Results for dynamic MWI of the thigh, using the semicircular array in MIMO mode, are shown in Fig. 6. Voxel intensity represent amplitude at the HR frequency, shown on a linear scale to emphasise peaks. The heatmap of spectral energy at the HR frequency [see Fig. 6(a)] shows a distinct peak at the location where the femoral artery is expected to be. Averaged time series M-mode data, with their voxel positions indicated using red squares in the heatmap image, are shown in Fig. 6(b) along with time-aligned ECG data. Unit of radar data is amplitude, which

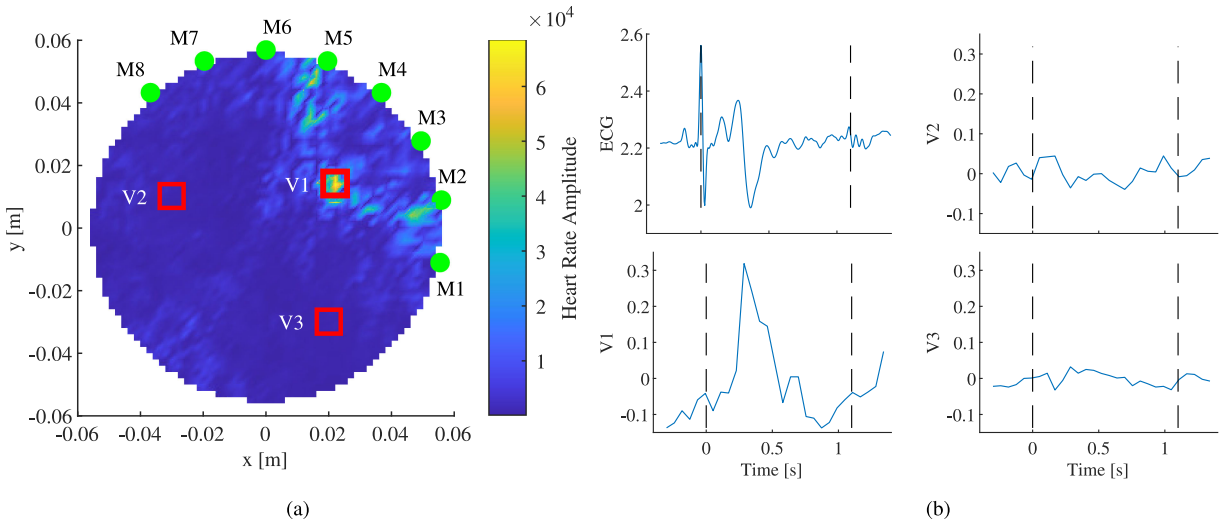

Fig. 6. Dynamic imaging result of a thigh cross-section, obtained using the semicircular antenna array, with all antennas acting as transmitter. The heatmap (a) shows activity at the heart rate frequency. M-mode time series (b) are shown for three voxels, indicated using red squares. M-mode data are time-aligned to electrocardiography (ECG) data (b); top left), dashed lines indicate the ECG R wave. Array antenna positions are denoted using green dots.

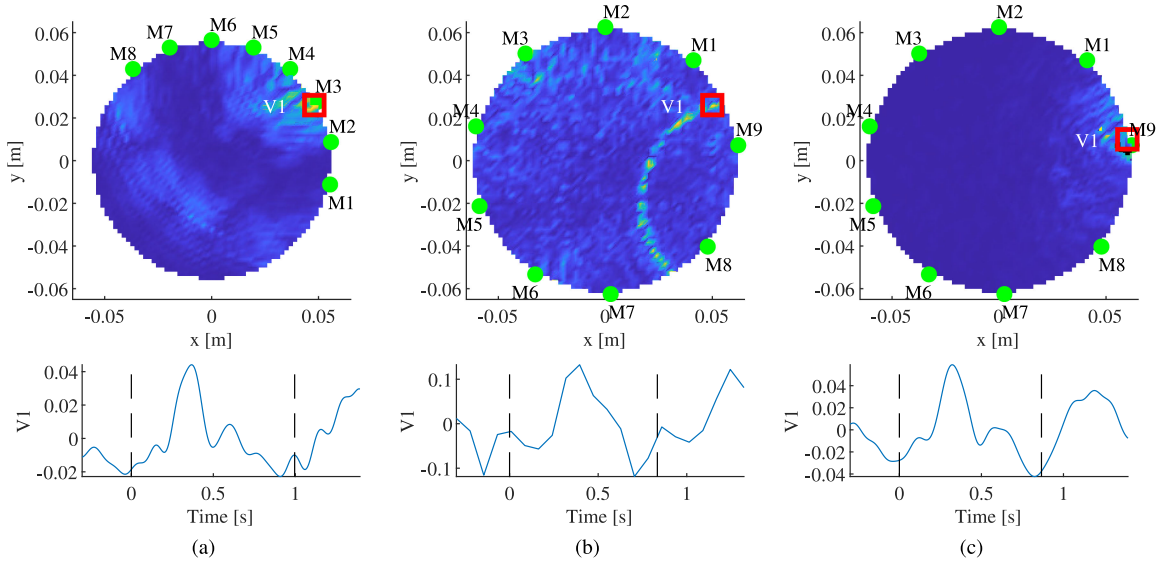

Fig. 7. Dynamic imaging result of a thigh cross-section, obtained using different antenna arrays, using either one or all antennas as transmitter. Both heatmap images (top) and electrocardiography (ECG) aligned M-mode time series (bottom) at red square indicators are shown. Dashed lines indicate the ECG R wave. Results are given for: Semicircular array, single transmitter (a); circular array, all antennas transmitting (b); and circular array, single transmitter (c).

is proportionate to sensor voltage. Dashed vertical lines indicate the timestamp of the averaged ECG R wave. Note that the second ECG R wave is not visible due to signal smearing as a result of averaging ECG signals with variable beat-to-beat intervals. The averaged M-mode signal at voxel V1 (at heatmap peak amplitude) shows a clear arterial pulse wave, whereas signals at V2 and V3 (voxels chosen at random locations) do not show the arterial pulse. Non-averaged time series (not shown) data showed similar responses for individual pulse waves, albeit with higher levels of noise.

Results of different recording conditions and settings are shown in Fig. 7, with both the heatmap image and corresponding averaged M-mode signal at the voxel with maximum amplitude (indicated using a red square). A SIMO mode recording using the semicircular array [see Fig. 7(a)] appeared to have an insufficient number of channels (factor 8 lower than for MIMO data) to resolve the femoral artery location. The lower number of Tx elements did result in a higher temporal resolution (sampling rate of 172 Hz as opposed to 17 Hz) with a better defined arterial pulse signal. A MIMO recording using the circular array [see Fig. 7(b)], suffered from a low number of channels containing HR data (compromising gain through channel summation). The detected signal peak is superficial to the skin, although a second and third highest peak (similar amplitude)

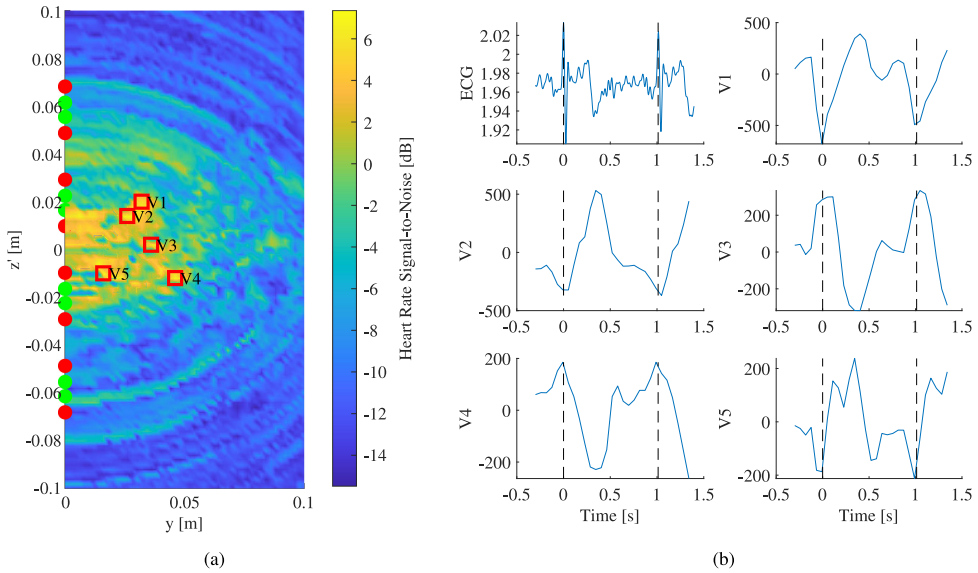

Fig. 8. Dynamic image of a cross-section of the heart, along its long axis, obtained from a rectangular antenna array pressed against the chest. The heatmap image (a) shows activity at the heart rate frequency. ECG data and radar M-mode time series data are shown (b) for five voxels of interest, indicated using red squares in (a). M-mode data are time-aligned to ECG data, dashed lines indicate the ECG R wave. The red and green dots in (a) indicate the positions of the receiving and transmitting antennas, respectively.

lie closer to hypothesized artery location. Circular array SIMO imaging [see Fig. 7(c)] again suffer from a low number of channels containing the HR signal, leading to an unresolved location of the measured arterial pulse wave. Static imaging at direct current (DC) did not result in imaging of the femur bone or any other identifiable anatomical structure (image not shown).

B. Heart Imaging

Dynamic imaging results for data collected from the chest, are shown in Fig. 8 for the cardiac long axis. Voxel intensity represents SNR at the HR frequency, represented in dB. SNR was plotted as opposed to amplitude at the HR frequency, because attenuation compensation in the rectangular array lead to excessively large signal amplitude at furthest voxels, complicating visualisation. Imaging results for the short axis (not shown) were similar. Clear periodic signals at the HR frequency are distinguishable, with averaged M-mode signals at different anatomical positions showing various temporal characteristics.

C. Phantom Imaging

Phantom differential imaging results are shown in Fig. 9 on a logarithmic scale, with a single target (a) and two targets (b). Target locations are indicated using red squares. Static imaging (no 'empty' data subtraction) did not result in identifiable targets in the obtained images. The resultant 'skin artefact' and antenna crosstalk after clutter rejection exceeded the amplitude of the signal of interest, and could not be filtered out as in dynamic imaging. A differential imaging approach was taken to produce results in Fig. 9. Due to a recording error, data from one of the RoC devices (M5 in Fig 2(c)) were lost. For the single target scenario, target location was correctly identified from the image

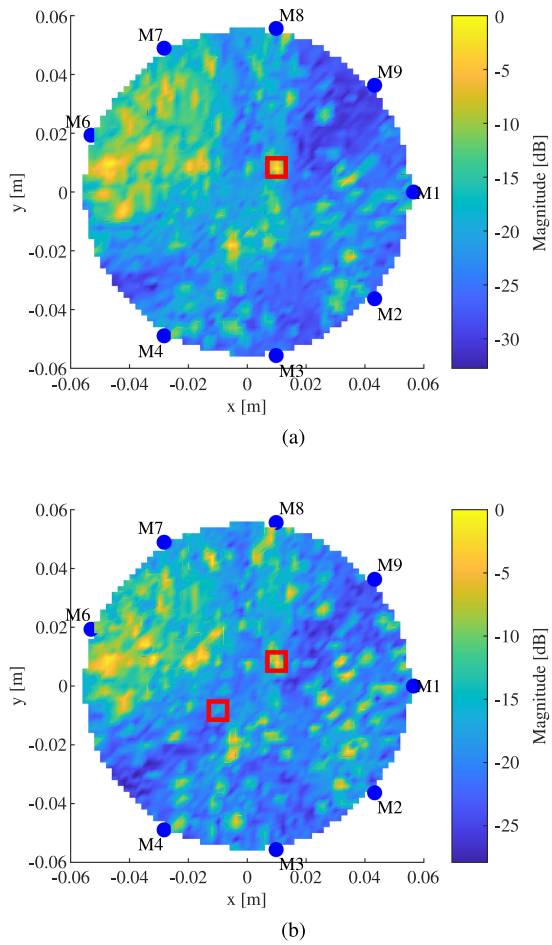

Fig. 9. Differential image of a phantom cross-section, with one (a) and two (b) metal bolts acting as imaging targets. Target locations are marked using red squares, array antenna positions are denoted using blue dots.

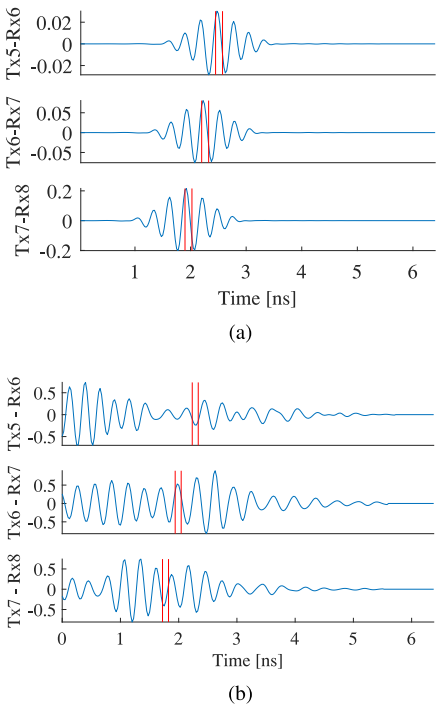

Fig. 10. Example of phantom imaging radar data prior to beamforming, from simulations (a) and experiments (b), both after subtraction of an empty-phantom recording. The focal point corresponding to the target location is indicated with red lines.

maximum SCR, with an SCR of 15.1 dB. However, substantial peaks of similar SCR were observed at locations not corresponding to a target. When a total of two targets were inserted, only the first target was successfully identified from image maximum SCR, albeit at reduced SCR. With three targets inserted, none of the targets could be identified (result not shown). It was observed that the differential image showed increased clutter amplitude near modules 6 and 7, indicating that the image with targets had diverged from the 'empty' image, as more targets were inserted in the phantom.

To explore the problem of target identification further, radar signals after differential clutter rejection are plotted in Fig. 10, for a subset of three geometrically similar channels. Red lines indicate the focus point for the voxel containing a target. Simulated data [see Fig. 10(a)] show the expected signal peak at the focus point, whereas experimental phantom data [see Fig. 10(b)] show noise across the radar frame. Expected signal peak-to-peak (P2P) amplitude was estimated, by considering transmitted P2P amplitude (measured), coupling loss (estimated from phantom data) and attenuation loss (predicted from numerical model data). For the three channels displayed in Fig. 10(b), the P2P amplitude was estimated at 0.16, 0.34, and 0.86, top to bottom. Estimates are in the order of magnitude of measured data, but noise appears to be present at similar or higher amplitudes.

IV. Discussion

A. Experimental Results

1) Thigh Imaging: Imaging of the thigh was performed as a first proof of concept of in-body RoC MWI in a relatively simple anatomical structure, with the femoral artery and femur bone acting as dynamic and static targets, respectively. Static imaging in the body proved unsuccessful. The dielectric contrast of bone in muscle tissue is low compared to the contrast caused by the metal bolts in the phantom, and differential imaging could not be performed. Significant improvements to clutter rejection are required to make static imaging with the current setup a reality. Dynamic imaging proved successful under certain conditions. Using the semicircular array in MIMO mode, a clear peak in HR amplitude was observed which corresponded to the hypothesized femoral artery position. The M-mode signal at the identified peak showed a plausible arterial pulse waveform, with clearly identifiable ejected wave, reflected wave and dicrotic notch [30]. In semicircular array MIMO data, the HR signal could be observed in 16 out of 64 channels, mostly between the four modules nearest to the artery. SIMO data performed worse, likely due to the lower number of channels and resulting reduced array gain. The use of a single Tx in case of SIMO data acquisition did result in a higher temporal resolution arterial pulse wave. For data collected using the circular array, the target location could not be resolved. Both for MIMO and SIMO data, the number of channels containing the HR signal was low.

For successful in-body imaging, a key consideration is the number of channels that can sense the anatomical structure of interest with sufficient SNR, which provides array gain through coherent summation. Channel dynamic range must be sufficient to capture the highly attenuated signal. Based on thigh measurements, an assessment was made of SNR. In individual channels, signal was considered the magnitude at the heart rate frequency, measured across slow-time, at a range bin (focal point) corresponding to measured artery location. Strongest static clutter signals were observed at low range bins, likely originating from antenna coupling. Noise was thus defined as magnitude at DC, measured at low range bins (prior to clutter suppression techniques in software). In channels where heart rate was discernable, an SNR was found ranging from 65 – 75 dB. Considering signal attenuation of around 5.2 dB/cm, and a measured receiver dynamic range around 80 dB (at high frame rates, depending on receiver settings), it is not unexpected that high path length channels fail to contribute to dynamic imaging in the current system.

2) Heart Imaging: Heart imaging was attempted to explore the challenges of a potential future clinical application of dynamic MWI. Data were collected using a rectangular array, along the heart's long and short axis. Results show that mechanical motion at the HR frequency is detected at the location where the heart is known to be. M-mode signals were periodic and peaks were found to align with ECG data, indicating that signals originated from cardiac motion. Although the HR signal was also detected at superficial positions (potentially caused by chest wall motion), highest signal strength was observed at a depth of 3 – 4 cm. Despite the detection of different M-mode signals from voxels corresponding to the heart location, it is uncertain to what extent actual imaging was successful. Beamforming relied on various assumptions concerning anatomy and tissue properties, and assumed a homogeneous medium. In reality, the complex anatomy of the rib cage and high velocity of moving structures in the heart, along with a lack of clearly distinguishable anatomical features in obtained images, make it challenging to interpret the results. Some M-mode signals

clearly resemble the Wiggers schematic diagram of cardiac dynamics [31]: Both the atrial filling of the ventricle upon the ECG P wave, and ventricle contraction upon the R wave appear to be visible through transient high amplitude signals. For some voxels, a slight delay relative to the R wave is observed, which could represent ventricular ejection delay. It is likely that signals were modulated by various cardiac anatomical structures, but identifying these structures based on voxel activity would be premature. Substantial improvements in spatial resolution and sensitivity, as well as anatomical model assumptions, are likely needed for RoC MWI to become a clinically relevant tool for the assessment of cardiac anatomy and mechanical function.

3) Phantom Imaging: Phantom imaging was performed to verify correct beamforming in a controlled environment, and to help understand limitations of the current system. Successful identification of the first target in the cylindrical phantom is encouraging, and demonstrates correct beamforming and the system's ability of differential imaging in lossy media. However, the inability to suppress additional peaks at similar amplitude (at non-target locations) illustrate the challenge when motion cannot be used to discern between target and clutter. Missing data from the module nearest to the second target could help explain the inability to identify target 2. A single phantom was used and modified throughout the experiment, causing alteration to the antenna-phantom interface and overall phantom volume, inflicted by insertion of the targets. The use of multiple phantoms for future experimentationis recommended. Estimates of expected P2P amplitude are encouraging: Measured signals are in the order of magnitude of estimated signal amplitude, suggesting that coherent summation gain should allow for resolving a target, particularly at higher channel counts.

B. Challenges and Opportunities of Using RoC Technology for MWI

Although MWI has been researched intensively, the current work was the first to demonstrate the use of RoC devices for this purpose. Compared to traditional radar systems and existing MWI devices, higher imaging speeds are achieved through synchronous data collection from multiple RoCs, providing the opportunity of dynamic imaging. High speed imaging could in theory be achieved using VNA systems with a large number of ports. However, with large array sizes, the cost and size of multi-port VNAs would quickly become prohibitive for various applications, and any VNA-based systems would sacrifice in sensitivity when operating at scanning times that were achieved in the current work. As an alternative imaging modality, ultrasound has been well established for imaging of cardiovascular dynamics. However, MWI has the advantage of better penetration through bone tissue, which could obviate the need for an experienced operator. In combination with high mobility and low-cost hardware, this could make RoC MWI a more attractive choice for long term and preventive monitoring outside the hospital setting. A number of challenges related to the current system design became apparent, which are being explored below.

1) Multipath Clutter Signals and System Calibration: The majority of developed MWI prototypes comprise of static, non-portable systems. Often, a coupling liquid is used (as in [6], [8], [11]), both to improve radiation into tissue and to absorb multipath clutter signals such as backscattered energy and antenna cross talk. For static systems, antennas are fixed in an array, and components are not likely to move. Because of this, system imperfection can typically be calibrated for. A portable and modular system however, such as proposed in the current work, poses the following challenges:

1) No coupling liquid can be used for absorption of signal leakage, leading to increased multipath interference.
2) The environment cannot be calibrated for, and participant motion will cause interference through signal leakage reflections.
3) Any inconsistency in body-coupled antenna surface hampers skin artefact reduction efforts.
4) The adjustable antenna fixation system inevitably leads to inaccuracies in antenna position and orientation, hindering grouped average clutter rejection and beamforming.

To date, a small number of portable MWI systems has been developed. A hand-held device for breast imaging employs an antenna array built into a dome, which is separated from the breast coupling dome using a coupling liquid [10]. The coupling dome ensures a constant skin-device interface, whereas the antenna dome ensures system component fixation. This configuration allows for better calibration than was achieved in the current work. It is expected that backscattered signal and standing waves (due to high bandwidth) would form a challenge however. A second group has developed a wearable array in a bra for breast health monitoring [32]. Antennas are designed to be in direct skin contact and no absorbing coupling liquid is used. For image formation using the bra-based system, similar challenges as encountered in this work could be expected. More recently, a portable system was proposed, consisting of a circular, rotating antenna array, with no direct skin-antenna contact [33]. The system was validated in a controlled environment on a phantom object, after a calibration procedure. It is to be expected however, that when such a system were to be used as a portable system on human participants, similar levels of calibration would not be achievable.

2) Imaging Speed: The unique advantage of using synchronized RoC devices is high imaging speed on large MIMO datasets. In the current work, using nine transmitters, a frame rate of 13.0 Hz was achieved, without loss of sensitivity. Single-frame scanning time was thus far shorter than previously reported on MWI systems, which are typically in the order of minutes [4], [6], [7], [9]. Only [18] has reported visualising heart motion, but by creating a time-lapse video: A video sequence was constructed from consecutively taken still images using ECG-timestamps.

The current system, although not a MIMO radar in the conventional sense of the word, employs consecutive scanning of Tx elements to synthesize a 'MIMO' dataset. Frame rate is therefore inversely related to the number of Tx elements, but Rx elements can be added at no cost to imaging speed. A

larger array with additional array gain at the benefit of SNR and improved clutter rejection, can therefore be constructed whilst maintaining temporal resolution, although Tx elements must always be placed strategically in order to irradiate the entire anatomical structure.

When considering a single RoC module, further improvements in imaging speed are possible. Frame rate is a function of signal integration and required receiver dynamic range. To avoid potential signal truncation, a wide input range was used in the current study. With further reduction of signal leakage and estimates of expected signal amplitude at individual modules, receiver range could be set to a fraction of the current settings, with a proportionate increase in imaging frame rate.

3) Bandwidth and Center Frequency: A time domain UWB RoC system provides less flexibility in pulse parameters selection than conventional systems such as a VNA. Assuming fixed array size (usually limited by constraints of anatomical geometry), center frequency and bandwidth of a radar imaging system determine its spatial resolution in cross-range and down-range, respectively. To improve spatial resolution, high center frequency and high pulse bandwidth would be preferred in theory. An increase in pulse center frequency also allows for a smaller antenna size, resulting in a higher number of antennas that can be fitted around a geometry and therefore potentially higher array gain. However, a high center frequency also comes at a cost of increased signal attenuation. Apart from reduced SNR, this leads to a lower number of channels being able to discern a target, and thus a lower effective aperture. Similarly to synthetic aperture radar principles, a large aperture (or array dimension) is beneficial for cross-range resolution. Whereas spatial resolution using circular arrays (as in breast imaging) is determined entirely by cross-range resolution, rectangular array imaging (such as for the cardiac scenario) relies both on effective aperture size for cross-range, and high bandwidth for down-range resolution. It is evident that optimal center frequency and bandwidth are dependent on geometry, and application specific RoC systems are likely required to reach clinically viable products.

4) Array Density: In the current work, array density was limited by module dimensions. A future iteration of the RoC module could have the same footprint as a set of Tx and Rx antennas (2 by 5 cm), or even the same footprint of a single antenna (2 by 2 cm in the current work). A higher array density will lead to reduced aliasing and increased array gain, and thus better imaging performance. Increased crosstalk as a result of reduced inter-antenna distance could form a new challenge.

5) Clutter Rejection: Rejection of multipath clutter signals (skin artefact, reflected signal leakage, antenna crosstalk, creeping waves, and propagation through low loss fat layers) is imperative for successful static MWI. For dynamic imaging, significant clutter rejection is performed by high-pass filtering. Whether clutter can be eliminated through differential imaging, as in the phantom recording, is application dependent. In simulated data, only a small drop in performance was observed when using grouped averaging instead of differential clutter rejection. In experimental data, grouped average clutter rejection proved not to be sufficient for target identification in a cylindrical phantom. Grouped Woody average clutter rejection was found to outperform simple (non-aligned) grouped average clutter rejection, but visualization of radar data demonstrates that clutter is still the dominant signal component. In this work, grouped average clutter rejection was likely hampered by the choice of hardware, which provided far less backscattered signal absorption than conventional systems (such as [4], [6], [11]) and was found to be prone to movement artefacts. The largest gains in imaging performance for the here presented system are likely to be realized by improving clutter rejection, both in hardware and software. Topics for further research include the use of more advanced algorithms such principal component analysis (PCA)-based artefact removal [34], distant-based filtering using independent component analysis [35], as well as hardware improvements such as microwave absorbing foam materials and modifications that would facilitate successful grouped averaging.

6) Assumption of Anatomy and Tissue Properties: Correct estimates of tissue properties are key for successful beamforming. Considering the large variation in anatomy between individuals, this is likely a substantial source of error. Simulation experiments (results not shown) showed a drop in SCR of 3–4 dB when adding 10% error to medium permittivity in a circular array beamforming scenario. Increasing window length (step P12 in 4) accounts to some extent for incorrect tissue and medium property assumptions, and resulted in a reduced drop in SCR at increased window lengths. Future work should point out whether expected anatomical variations between individuals are prohibitive for imaging using standard assumptions, or whether individualization is required. When imaging a thigh or limb, individual parameter assessment as in [32] could be performed. Improvements could also be made by implementing a parameter optimization algorithm for permittivity assessment [36]. The chest is a much more complex geometry: Transmissive measurements won't be representative for the small volume of tissue between the skin and the heart, and there are no clear point scatterers for parameter optimization. In addition, the anatomy surrounding the sternum is complex and highly irregular across antennas. Future work could include experimentation with array position. Although the sternum has been found to be a good transmissive window for heart sensing, array placement beside the sternum would make the clutter space much more homogeneous. A depth-dependent permittivity model (previously proposed in [37]) could account for different volumes of lung tissue.

7) Beamforming Algorithm: In this work, the DAS and DMAS algorithms were used. DMAS was found to be highly successful at clutter rejection. With the current implementation, DMAS computation time was prohibitive for use on dynamic video data. A large body of research has been done on more advanced beamforming techniques such as adaptive algorithms [38] and super-resolution techniques [35]. A recommendation for future work is the development of a data-adaptive channel-quality factor for dynamic imaging, that could suppress (high path length) channels without dynamic content.

V. Conclusion

Dynamic MWI of the cardiovascular system has been demonstrated using a system of synchronized RoC devices and arrays of body-coupled antennas. The pulse wave of the femoral artery, and dynamics originating from the heart, were successfully imaged using the novel system. Due to the complexity of the chest anatomy, no individual cardiac structures could be identified from obtained images. The current work shows that RoC devices may provide several unique advantages over conventional MWI systems, such as high imaging speed, low cost, small form factor, and portability. However, as the system was primarily designed for dynamic imaging, static and differential imaging in the body proved unsuccessful. This illustrates a challenge of building a modular and portable MWI system: The inability to calibrate for all system imperfections and absence of clutter suppressing features (such as coupling liquids) make that static imaging can only be done in highly controlled environments. This of course is a characteristic of any portable MWI system, and is not due to the use of RoC devices. RoC technology does have the potential to make MWI devices available at low cost and small form factor, and high imaging speeds make that this could in the future provide an alternative medical imaging modality for dynamic systems such as the heart and vascular system.

References

[1] D. O'Loughlin *et al.*, "Microwave breast imaging: Clinical advances and remaining challenges," *IEEE Trans. Biomed. Eng.*, vol. 65, no. 11, pp. 2580–2590, Nov. 2018.

[2] M. Persson *et al.*, "Microwave-based stroke diagnosis making global prehospital thrombolytic treatment possible," *IEEE Trans. Biomed. Eng.*, vol. 61, no. 11, pp. 2806–2817, 2014.

[3] K. Foster and H. P. Schwan, "Dielectric properties of tissues and biological materials: A critical review," *Crit. Rev. Biomed. Eng.*, vol. 17, pp. 25–104, Feb. 1989.

[4] J. Bourqui, J. Sill, and E. Fear, "A prototype system for measuring microwave frequency reflections from the breast," *Int. J. Biomed. Imag.*, vol. 2012, p. 12, 2012.

[5] A. Mobashsher *et al.*, "Design and experimental evaluation of a non-invasive microwave head imaging system for intracranial haemorrhage detection," *PLoS ONE*, vol. 11, no. 4, 2016, Art. no. e0152351.

[6] M. Shere *et al.*, "MARIA M5: A multicentre clinical study to evaluate the ability of the micrima radio-wave radar breast imaging system (MARIA) to detect lesions in the symptomatic breast," *Eur. J. Radiol.*, vol. 116, pp. 61–67, 2019.

[7] E. Porter, M. Coates, and M. Popovic, "An early clinical study of time-domain microwave radar for breast health monitoring," *IEEE Trans. Biomed. Eng.*, vol. 63, no. 3, pp. 530–539, Mar. 2016.

[8] P. Meaney *et al.*, "A clinical prototype for active microwave imaging of the breast," *IEEE Trans Microw. Theory Techn.*, vol. 48, no. 11, pp. 1841–1853, 2000.

[9] M. Hopfer *et al.*, "Electromagnetic tomography for detection, differentiation, and monitoring of brain stroke," *IEEE Ant. Prop. Mag.*, vol. 59, no. 5, pp. 86–97, Aug. 2017.

[10] H. Song *et al.*, "Detectability of breast tumor by a hand-held impulse-radar detector: Performance evaluation and pilot clinical study," *Sci. Rep.*, vol. 7, no. 1, 2017, Art. no. 16353. [Online]. Available: https://doi.org/10.1038/s41598-017-16617-6

[11] A. Fasoula *et al.*, "On-site validation of a microwave breast imaging system, before first patient study," *Diagnostics*, vol. 8, no. 3, p. 53, 2018.

[12] F. Yang *et al.*, "A large-scale clinical trial of radar-based microwave breast imaging for asian women: Phase I," in *Proc. IEEE Int. Symp. Ant. Prop.*, 2017, pp. 781–783.

[13] T. Lauteslager *et al.*, "Coherent uwb radar-on-chip for in-body measurement of cardiovascular dynamics," *IEEE Trans. Biomed. Circuits Syst.*, vol. 13, no. 5, pp. 814–824, Oct. 2019.

[14] K. G. Kjelgård *et al.*, "Heart wall velocity sensing using pulsed radar," in *Proc. Conf. IEEE Biomed. Circuits Syst.*, 2017, pp. 1–4.

[15] E. Schires, P. Georgiou, and T. Lande, "Vital sign monitoring through the back using an UWB impulse radar with body coupled antennas," *IEEE Trans. Biomed. Circuits Syst.*, vol. 12, no. 2, pp. 292–302, Apr. 2018.

[16] D. Buxi, J. Redouté, and M. Yuce, "Blood pressure estimation using pulse transit time from bioimpedance and continuous wave radar," *IEEE Trans Biomed Eng*, vol. 64, no. 4, pp. 917–927, Apr. 2017.

[17] Y. Kuwahara, "Microwave imaging for early breast cancer detection," in *Breast Imag.*, Rijeka: IntechOpen, 2017.

[18] S. Brovoll *et al.*, "Time-lapse imaging of human heart motion with switched array UWB radar," *IEEE Trans. Biomed. Circuits Syst.*, vol. 8, no. 5, pp. 704–715, Oct. 2014.

[19] E. Madsen, J. Zagzebski, and G. Frank, "Oil-in-gelatin dispersions for use as ultrasonically tissue-mimicking materials," *Ultrasound Med. Biol.*, vol. 8, no. 3, pp. 277–287, 1982.

[20] M. Lazebnik *et al.*, "Tissue-mimicking phantom materials for narrowband and ultrawideband microwave applications," *Phys. Med. Biol.*, vol. 50, no. 18, 2005, Art. no. 4245.

[21] H. Hjortland and T. Lande, "CTBV integrated impulse radio design for biomedical applications," *IEEE Trans. Biomed. Circuits Syst.*, vol. 3, no. 2, pp. 79–88, 2009.

[22] M. Tømmer, K. G. Kjelgård, and T. S. Lande, "Body coupled wideband monopole antenna," in *IEEE Loughborough Ant. Prop. Conf.*, Nov. 2016, pp. 1–5.

[23] P. Hasgall *et al.*, "It'is database for thermal and electromagnetic parameters of biological tissues," Version 4, May 2018.

[24] S. Brovoll *et al.*, "Optimal frequency range for medical radar measurements of human heartbeats using body-contact radar," in *Proc. Conf. Proc. IEEE Eng. Med. Biol. Soc.*, 2013, pp. 1752–1755.

[25] Visible Human Project, Courtesy of the U.S. National Library of Medicine. Accessed: 21 Mar., 2022. [Online]. Available: https://www.nlm.nih.gov/research/visible/

[26] H. Kanehisa, S. Ikegawa, and T. Fukunaga, "Comparison of muscle cross-sectional area and strength between untrained women and men," *Eur J. Appl Physiol*, vol. 68, no. 2, pp. 148–154, 1994.

[27] M. Fernando *et al.*, "Fundamental issues in antenna design for microwave medical imaging applications," in *Proc. Int. Symp. Commun. Syst. Netw. Dig. Signal*, 2010, pp. 795–800.

[28] E. Fear *et al.*, "Confocal microwave imaging for breast cancer detection: Localization of tumors in three dimensions," *IEEE Trans. Biomed. Eng.*, vol. 49, no. 8, pp. 812–822, Aug. 2002.

[29] L. Hooi Been *et al.*, "Confocal microwave imaging for breast cancer detection: Delay-multiply-and-sum image reconstruction algorithm," *IEEE Trans. Biomed. Eng.*, vol. 55, no. 6, pp. 1697–1704, Jun. 2008.

[30] M. O'Rourke, A. Pauca, and X. Jiang, "Pulse wave analysis," *Brit. J. Clin. Pharmacol*, vol. 51, no. 6, pp. 507–522, 2001.

[31] J. Mitchell and J.-J. Wang, "Expanding application of the wiggers diagram to teach cardiovascular physiology," *Adv. Physiol. Educ.*, vol. 38, no. 2, pp. 170–175, 2014.

[32] E. Porter *et al.*, "A wearable microwave antenna array for time-domain breast tumor screening," *IEEE Trans. Med. Imag.*, vol. 35, no. 6, pp. 1501–1509, Jun. 2016.

[33] M. T. Islam *et al.*, "A low cost and portable microwave imaging system for breast tumor detection using UWB directional antenna array," *Sci. Rep.*, vol. 9, no. 1, pp. 1–13, 2019.

[34] E. Ricci *et al.*, "Pca-based artifact removal algorithm for stroke detection using UWB radar imaging," *Med. Biol. Eng. Comput.*, vol. 55, no. 6, pp. 909–921, 2017.

[35] A. Fasoula *et al.*, "Super-resolution radar imaging for breast cancer detection with microwaves: The integrated information selection criteria," in *Conf. Proc. IEEE Eng. Med. Biol. Soc.*, 2019, pp. 1868–1874.

[36] D. O'Loughlin *et al.*, "Advantages and disadvantages of parameter search algorithms for permittivity estimation for microwave breast imaging," in *Conf. Proc. Eur. Conf. Ant. Prop.*, 2019, pp. 1–5.

[37] A. Mobashsher, A. Mahmoud, and A. Abbosh, "Portable wideband microwave imaging system for intracranial hemorrhage detection using improved back-projection algorithm with model of effective head permittivity," *Sci. Rep.*, vol. 6, 2016, Art. no. 20459.

[38] M. Elahi *et al.*, "Evaluation of image reconstruction algorithms for confocal microwave imaging: Application to patient data," *Sensors*, vol. 18, no. 6, p. 1678, 2018.